Coupled Dipole Modeling and Experimental Characterization of Geometry-Dependent Trochoidal Dichroism in Nanorod Trimers

Rashad Baiyasi,^a Harrison J. Goldwyn,^b Lauren A. McCarthy,^c Claire A. West,^b Seyyed Ali Hosseini Jebeli,^a David J. Masiello,*^b Stephan Link,*^{a,c,d} Christy F. Landes*^{a,c,d,e}

^aDepartment of Electrical and Computer Engineering, Rice University, MS 366, Houston, Texas 77005, United States

^bDepartment of Chemistry, University of Washington, Seattle, Washington 98195, United States ^cDepartment of Chemistry, Rice University, MS 60, Houston, Texas 77005, United States ^dSmalley-Curl Institute, Rice University, Houston, Texas 77005, United States ^eDepartment of Chemical and Biomolecular Engineering, Rice University, Houston, Texas 77005, United States

Abstract

Noble metal nanoparticles host surface plasmon resonances that confine electromagnetic waves below the diffraction limit of light, making them effective building blocks for near-field optical antennas. Efficient prediction and design of nanoantenna systems are facilitated by improved understanding of their optical properties. Here, we utilize an intuitive coupled-dipole model for fan-shaped gold nanorod trimers together with experiment to investigate the role of near- and far-field effects upon optical dichroism using both linear and trochoidal polarizations with

cartwheeling field motion matching the geometry of the trimers. Our coupled-dipole model predicts the linear and trochoidal dichroism that we observe in experiments, and we demonstrate that trochoidal intensity modulation can be tuned and reversed by varying the geometric parameters of the gold nanorod trimers. Simple analytical models, coupled with easily understood visualizations, provide a useful framework for predictive nanoantenna design applications.

KEYWORDS plasmonics, optical antenna, coupled-dipole model, nanorod, trochoidal dichroism, predictive nanoantenna design

Coherent excitations of conduction band electrons known as plasmons confine free-space radiation to the nanoscale, a size regime inaccessible via traditional optics. The plasmon resonances of noble metal nanoantennas often lie within the visible spectrum and can be tuned by altering the geometry or local environment. A wide range of nanoantenna designs can be realized with modern top-down³⁻⁶ and bottom-up⁷ fabrication techniques, with varied applications including molecular sensing, and bottom-up⁷ fabrication techniques, with varied applications including molecular sensing, and bottom-up⁷ fabrication techniques, with varied applications including molecular sensing, and bottom-up⁷ fabrication techniques, with varied applications including molecular sensing, and bottom-up⁷ fabrication techniques, with varied applications including molecular sensing, and bottom-up⁷ fabrication techniques, with varied applications including molecular sensing, and bottom-up⁷ fabrication techniques, with varied applications including molecular sensing, and bottom-up⁷ fabrication techniques, with varied applications including molecular sensing, and bottom-up⁷ fabrication techniques, with varied applications including molecular sensing, and bottom-up⁷ fabrication techniques, with varied applications including molecular sensing, and bottom-up⁷ fabrication techniques, with varied applications including molecular sensing, and bottom-up⁷ fabrication techniques, with varied applications including molecular sensing, and bottom-up⁷ fabrication techniques, with varied applications including molecular sensing, and bottom-up⁷ fabrication techniques, and are realized with modern top-down³⁻⁶ on the including molecular sensing, and the sensing and bottom-up⁷ fabrication techniques, and are realized with modern top-down³⁻⁶ on the including molecular sensing, and the sensing and the sensin

The drive for efficient design and implementation of optical antennas motivates the development of methodologies for understanding and predicting their optical properties. While optical antennas draw natural comparisons to classical radio-frequency antennas, the difference in size regimes prevents the direct application of modern antenna theory to the nanoscale.⁴¹ Numerical simulation methods, such as

finite-difference time-domain (FDTD) and the finite element method are often used to predict nanoantenna properties and verify experimental results.^{27, 32, 39} Though robust numerical simulations provide some level of understanding,^{27, 39} simple analytical models can offer insight about the underlying mechanisms driving optical properties.

One framework that has been successfully applied to plasmonic nanoantennas is the coupled-dipole model, in which plasmon resonances are treated as damped and driven oscillators. ^{28, 33, 42-46} These models can explain nanoantenna phenomena such as circular dichroism^{33, 46} and the shifting of molecular point spread functions. ⁴³ They have also aided in informing the design of tailored polarization dependent optics. With the continually expanding range and precision of fabrication techniques, including lithography, ^{30, 32} chemical synthesis, ⁴⁷⁻⁴⁹ and controlled assembly, ^{7, 31, 34, 50-53} deeper understandings of optical behaviors are needed to facilitate the systematic design of nanoantenna complexes tailored to specific applications.

In this manuscript, we use a reduced-order coupled-dipole model to interpret the polarization dependent scattering of fan-shaped gold nanorod trimers (AuNRTs). The model is used to investigate optical dichroism under both linear and trochoidal polarizations, the latter characterized by cartwheeling field motion. By separating between near- and far-field effects, the model reveals that modulation of polarization dependent scattering intensity is predominantly a consequence of far-field interference between nanorod scatterers. With these insights, we predict the design of a reversed intensity modulation AuNRT nanoantenna. This work highlights the importance of considering both near- and far-field effects in nanoantenna design and demonstrates the predictive power of intuitive theoretical models.

Modeling AuNRT Light-Matter Interactions

A scanning electron microscope (SEM) micrograph of a lithographically fabricated AuNRT on an indium tin oxide (ITO)-coated glass coverslip is shown in Figure 1a. The constituent 80 x 40 x 40 nm nanorods are arranged in a fan shape with 20 nm corner-to-corner gaps and an angular offset of 45°,

meaning that the side nanorods are oriented $\pm 45^{\circ}$ relative to the central nanorod. Each nanorod is modeled as a 1D point dipole oscillator coupled to its nearest neighbors via the electric dipole field. This model is illustrated in Figure 1b as a ball-and-spring system, where the springs connecting the balls represent the near-field coupling between oscillators. Two approximations keep the model simple and analytical: the point dipole oscillations are restricted to the long axis of their respective nanorods, and each dipole is coupled to its nearest neighbors only.

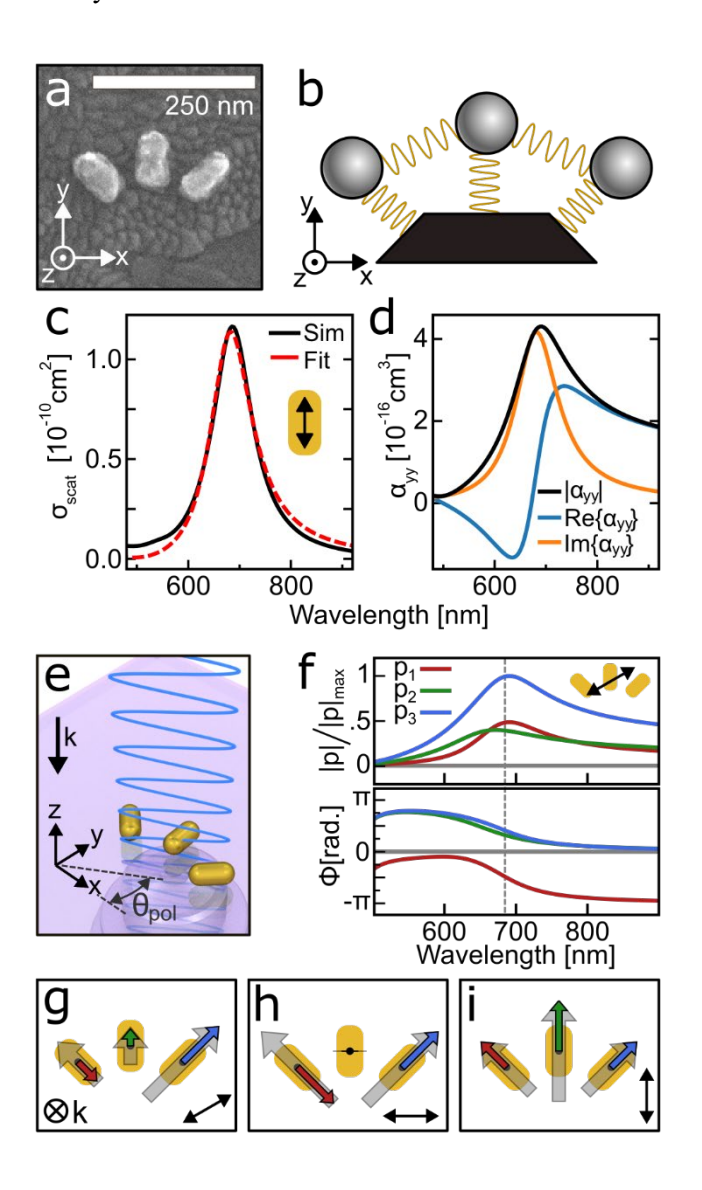


Figure 1. A coupled-dipole model of the near-field interactions in AuNRTs. (a) SEM micrograph of lithographically prepared AuNRT with 20 nm corner-to-corner gaps and side nanorods oriented at 45° relative to the center. (b) Ball-and-spring diagram of the coupled-dipole model. Each nanorod is treated

as a 1D oscillator and adjacent nanorods couple in the near field. (c) Single nanorod longitudinal mode scattering cross-section calculated by FDTD simulation (black) and fit to a parameterized model (dashed red). (d) Magnitude (black), real component (blue), and imaginary component (orange) of the nanorod polarizability obtained from fitting in (c). (e) Normal incidence excitation geometry for a linearly polarized source. (f) Calculated oscillation amplitude (top) and phase (bottom) as a function of wavelength for dipoles 1 (red), 2 (green), and 3 (blue) under plane wave excitation polarized at 30° (inset). (g-i) Dipole state diagrams overlaid on the AuNRT geometry for 685 nm excitation polarized at 30° (g), 0° (h), and 90° (i). The polarization angle relative to the AuNRT geometry is indicated in the bottom-right corner. Each dipole moment is represented by its full oscillation range in both directions (grey arrow) and the real component of the dipole moment (colored arrow), which can be understood as a snapshot of the oscillating dipoles.

The anisotropic polarizability tensor $\alpha(\omega)$ describes the dipole moment oscillation induced by an electric field of frequency ω . For nanorod antennas, we take $\alpha(\omega)$ to be that of a prolate spheroid in the modified long-wavelength approximation as derived in Ref. 54 and used in the same context as this manuscript in Ref. 28. Assuming a Drude dielectric function for Au, the frequency-dependent polarizability is determined by six parameters: $(\varepsilon_{\infty}, \omega_p, \gamma, a, b, \varepsilon_b)$. The first three are material properties inherent to the Drude model, where ε_{∞} is the high-frequency limit of the dielectric function, ω_p is the characteristic plasma frequency of electron gas oscillation, and the damping constant γ accounts for electric-ion scattering in bulk. The semi-radii of the spheroid, α and α and α are included as free geometric parameters as the spheroid is an approximation of the fabricated rod geometry. The surrounding medium dielectric constant, ε_b , is also varied to account for the experimental substrate, which is not explicitly included in this model (see Supplementary Note 1). By simultaneously fitting the modeled scattering cross sections of the longitudinal and transverse resonances to the corresponding resonances from FDTD simulations (Figure 1c, Figure S-1) we obtain the polarizability of each rod as a function of frequency, $\alpha(\omega; \varepsilon_{\infty}, \omega_p, \gamma, a, b, \varepsilon_b)$, shown in Figure 1d. Due to the spectral separation from the longitudinal mode and low relative intensity of the transverse mode, we were able to sufficiently model

the optical properties of the AuNRTs by retaining only the longitudinal polarizability element, motivating our use of a 1D oscillator for each nanorod. Further details on the polarizability model can be found in Supplementary Note 1 and Figure S-2. While the smallest nanorod separation studied here is 20 nm, boundary element method simulations (Figure S-3) demonstrate that the coupled-dipole model approximates coupled nanorods for separations down to 1 nm. The small variations seen in resonance peak wavelength do not qualitatively change our understanding of the system.

Light scattering from the AuNRTs is expressed as a set of coupled-dipole equations. The induced dipole moment in nanorod i, \mathbf{p}_i , centered at position \mathbf{r}_i is $\mathbf{p}_i = \boldsymbol{\alpha} \cdot \mathbf{E}(\mathbf{r}_i)$, where \mathbf{E} is the total electric field accounting for the external driving field, \mathbf{E}_F , as well as the near field generated by the other dipoles, \mathbf{E}_j , labeled j. The resulting coupled-dipole equations are

$$\mathbf{p}_i = \alpha [\mathbf{E}_{\mathrm{F}}(\mathbf{r}_i) + \Sigma_{i \neq i} \mathbf{E}_i(\mathbf{r}_i)], \tag{1}$$

where the subscript i, j = 1, 2, 3 indexes the nanorods from left to right, respectively. The field at position \mathbf{r}_i due to dipole \mathbf{p}_j is $\mathbf{E}_j(\mathbf{r}_i) = \mathbf{G}(\mathbf{r}_i, \mathbf{r}_j) \cdot \mathbf{p}_j$, where \mathbf{G} is the standard dyadic Green's function of a dipole source (Supplementary Note 2).⁵⁵ To obtain an analytical solution, we restrict to nearest neighbor coupling, resulting in the simplified equations

$$\mathbf{p}_{1} = \alpha [\mathbf{E}_{F}(\mathbf{r}_{1}) + \mathbf{E}_{2}(\mathbf{r}_{1})] \tag{2}$$

$$\mathbf{p}_2 = \alpha [\mathbf{E}_F(\mathbf{r}_2) + \mathbf{E}_1(\mathbf{r}_2) + \mathbf{E}_3(\mathbf{r}_2)]$$
 (3)

$$\mathbf{p}_3 = \alpha [\mathbf{E}_F(\mathbf{r}_3) + \mathbf{E}_2(\mathbf{r}_3)]$$
 (4)

By substituting **G** into Equations (2-4), the system of equations can be solved to determine the induced dipole moment

$$\mathbf{p}_{2} = [\mathbb{I} - \alpha \mathbf{G}_{21} \alpha \mathbf{G}_{12} - \alpha \mathbf{G}_{23} \alpha \mathbf{G}_{32}]^{-1} \alpha$$

$$\cdot [\mathbf{G}_{21} \alpha \mathbf{E}_{F}(\mathbf{r}_{1}) + \mathbf{G}_{23} \alpha \mathbf{E}_{F}(\mathbf{r}_{3}) + \mathbf{E}_{F}(\mathbf{r}_{2})]$$
(5)

of the central oscillator, where $\mathbf{G}_{ij} = \mathbf{G}(\mathbf{r}_i, \mathbf{r}_j)$ and \mathbb{I} is the 3×3 identity matrix. The remaining dipole moments (i = 1 and 3) are calculated via $\mathbf{E}_2(\mathbf{r}_i) = \mathbf{G}(\mathbf{r}_i, \mathbf{r}_2) \cdot \mathbf{p}_2$.

For a normal incidence linearly polarized excitation geometry as in Figure 1e, the state of the dipole oscillators can be intuitively related to the polarization angle. Under 30° incident polarization, the oscillation amplitude of dipole 3 in the top plot of Figure 1f is ~2x greater than for dipoles 1 and 2. The greater amplitude of dipole 3 indicates that it is driven more strongly by the excitation, consistent with the close alignment between the long axis of nanorod 3 and the polarization vector. The relative phase among dipole oscillations is used to understand the response of the AuNRT system to incident polarization. For example, in Figure 1f, dipoles 2 and 3 oscillate almost completely in phase, while dipole 1 oscillates ~180° out of phase across the calculated spectrum. This relative phase configuration can be understood by noting that dipole 1 is almost orthogonal to the incident field and will be negligibly driven by the external field, while dipole 2 will influence dipole 1 into a head-to-tail configuration through near-field coupling. With both phase and amplitude, a clear picture of the oscillator behavior takes shape.

We represent the complex dipole moments as dipole state diagrams shown in Figure 1g-i to provide a visual understanding of the coupled oscillator system. Each point dipole can be written as $\mathbf{p}_i = p_i \hat{\mathbf{u}}_i$ for complex scalar p_i and unit vector $\hat{\mathbf{u}}_i$ directed along the nanorod long axis. Since the individual 1D point dipoles oscillate along fixed orientations, the AuNRT model can be completely described with the complex dipole state vector $\mathbf{p} = (p_1, p_2, p_3)$. We calculate the dipole state vectors in Figure 1g-i for different incident field polarization angles at the single nanorod longitudinal scattering maximum $\lambda = 685$ nm, indicated as a vertical dashed grey line in Figure 1f. The grey arrows in the dipole state diagrams represent the full range of oscillation in both directions, with lengths corresponding to $2|\mathbf{p}_i|^2$ and arrowheads pointing in the direction we define as 0° phase. The colored arrows, of length $Re\{\mathbf{p}_i\}$, represent a snapshot of the oscillating dipoles and provide an understanding of the relative phase of the complex dipole moments. For example, 0° phase points in the direction of the gray arrow, 180° phase points in the opposite direction, and at $\pm 90^\circ$ phases the dipole shrinks to a negligible size and is displayed as a straight line with no arrowhead.

The dipole state diagrams reveal the underlying behavior of the coupled oscillators in the AuNRT model under a linearly polarized incident field. For 30° incident polarization, Figure 1g shows the state of the oscillating dipoles without requiring the full amplitude and phase spectra of Figure 1f, specifically the largest oscillation amplitude displayed by dipole 3 and the ~180° out of phase oscillation of dipole 1. Inspecting the dipole state diagram in Figure 1h for 0° excitation polarization, we see that the vertically oriented dipole 2 is completely undriven. While dipole 2 is orthogonal to the incident polarization, it does have the potential to be driven by near-field coupling to its neighbors. But, because dipoles 1 and 3 oscillate with equivalent magnitudes 180° out of phase, their influence is equal and opposite. The dipole state diagram for the 90° excitation polarization in Figures 1i paints a simpler picture, one where all dipoles oscillate in phase and the dipole aligned with the polarization angle is driven with the largest oscillation amplitude.

Impact of Far-Field Interference

The AuNRT scattering spectra blue shift and increase in intensity as the polarization angle is increased. Figure 2a-b depicts the linearly polarized excitation geometry and the experimental and calculated scattering spectra for excitation polarizations ranging from 0° to 90° for 20 nm gap AuNRTs. Optical dichroism can be summarized in terms of variations to the scattering under changing polarization, and can manifest as pure intensity modulation, resonance shifts, or both. 35, 39-40, 56 As evident in Figure 2b, the AuNRTs exhibit both intensity modulation and spectral shift. At 0° linear polarization, the experimental scattering peak is at 690 nm, but by changing the polarization angle to 90° the resonance blue shifts to 670 nm while increasing in intensity by 41%. This trend is well-reproduced by the coupled-dipole model, included in the bottom panel of Figure 2b. The linearly polarized detection geometry used in experiment yields equivalent spectra to the linearly polarized excitation used in the coupled-dipole model due to reciprocity between the received and radiated light by optical antennas. 57-58 FDTD simulations for linearly polarized excitation produce the same trend in scattering intensity, validating the use of linearly polarized detection for experimental measurements (Figure S-4).

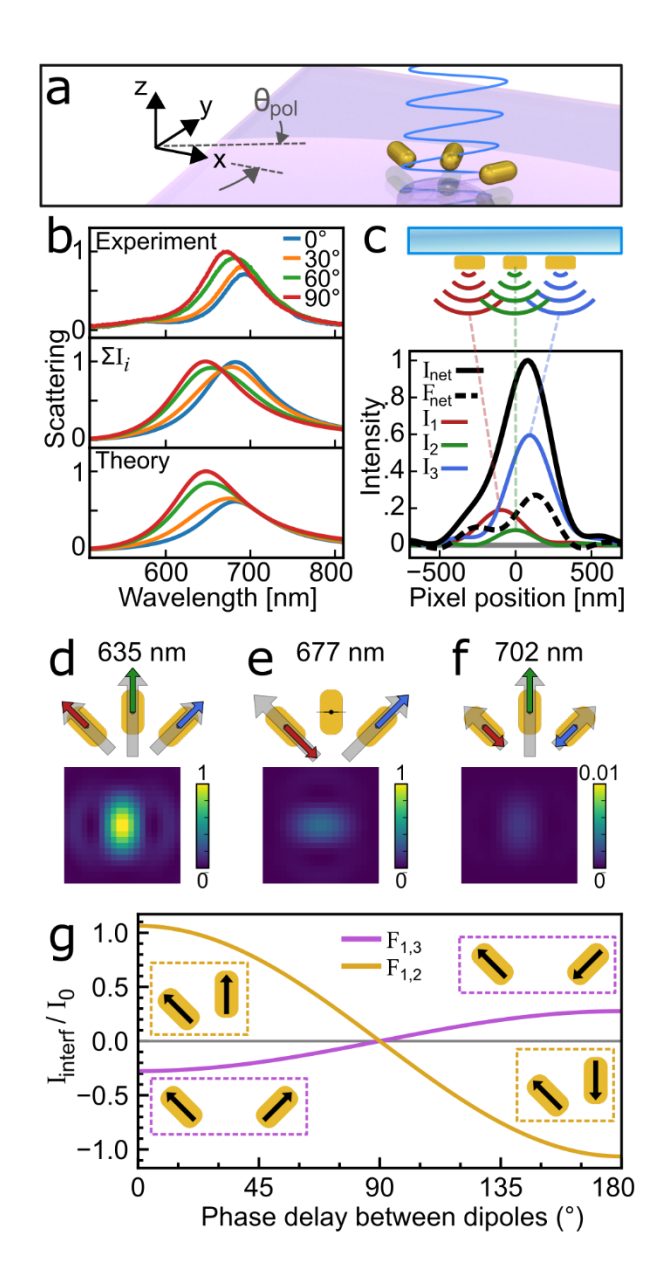


Figure 2. Far-field interference between oscillating dipoles modulates the intensity of scattering from AuNRTs. (a) Excitation geometry for linearly polarized normal incidence excitation source. (b)

Polarization dependent scattering of AuNRTs measured experimentally (top), calculated by summation of single-dipole intensities (middle), and calculated by our theoretical model including far-field interference (bottom). Scattering peak positions are reported in Table S-1. (c) Contributions to the scattering intensity measured in the image plane. The net scattering intensity (solid black) is the summation of the three dipole point spread functions (colored lines) and their interference (dashed black). (d-f) Dipole state diagrams and image plane intensity distributions of the normal modes of the AuNRT. The net intensity

decreases from high to low eigenfrequency modes (left to right) due to far-field interference, with the 702 nm mode intensity colormap being scaled $\times 0.01$ for visibility. (g) Interference between pairs of nanorods (inset) isolated from the AuNRT. Dipoles with an angular offset of 45° produce greater interference than those offset by 90°.

We calculate the diffraction-limited image fields generated by the model dipoles to bridge the gap between the coupled-dipole equations and the observed scattering intensity. The integrated scattering intensity is calculated from a discrete 20-by-20 grid of (x, y) coordinates spanning 1 μ m in the image plane. The intensity at each point in the image plane is proportional to the square magnitude of the focused electric field calculated by propagating the focused dipole fields to the image plane with the Debye-Wolfe diffraction integral.²⁸ For example, the *i*th dipole emitter produces an integrated intensity $I_i \propto \sum_{x,y} \left| \mathbf{E}_i^{\text{im}}(x,y) \right|^2$ in the image plane. For the remainder of this manuscript, the summation over the image plane positions $\sum_{x,y}$ is not written explicitly but should be assumed wherever integrated intensities are calculated from image plane fields.

Spectral shifts in AuNRTs can be reproduced by only considering near-field interactions, but the observed intensity modulation is predominantly a consequence of far-field interference effects. Since the scattering intensity of a single dipole, I_i , is proportional to its oscillation amplitude, the plot of $\sum I_i$ in Figure 2b represents how strongly the entire system is driven. The peak intensity of $\sum I_i$ blue shifts as the polarization angle becomes aligned with the AuNRT axis of symmetry but does not accurately calculate the changing scattering intensity seen in the experiment. By incorporating far-field interference, the coupled-dipole model (Figure 2b, bottom plot) reproduces both the spectral and intensity changes observed in experiment.

Far-field interference in the image plane modulates the scattering intensity based on the complex dipole state as shown in Figure 2c. The integrated scattering intensity in the image plane can be separated into six components,

$$I_{net} = \frac{cn}{8\pi} \left| \mathbf{E}_{1}^{\text{im}} + \mathbf{E}_{2}^{\text{im}} + \mathbf{E}_{3}^{\text{im}} \right|^{2}$$

$$= \frac{cn}{8\pi} \left[\left| \mathbf{E}_{1}^{\text{im}} \right|^{2} + \left| \mathbf{E}_{2}^{\text{im}} \right|^{2} + \left| \mathbf{E}_{3}^{\text{im}} \right|^{2} + 2\text{Re} \left\{ \mathbf{E}_{2}^{\text{im}} \mathbf{E}_{3}^{\text{im}^{*}} \right\} + 2Re \left\{ \mathbf{E}_{3}^{\text{im}} \mathbf{E}_{1}^{\text{im}^{*}} \right\} + 2Re \left\{ \mathbf{E}_{1}^{\text{im}} \mathbf{E}_{2}^{\text{im}^{*}} \right\} \right]$$
(6)

where n is the ambient refractive index, c is the speed of light in vacuum, and * denotes complex conjugation. It can be written succinctly as

$$I_{net} = I_1 + I_2 + I_3 + F_{2,3} + F_{3,1} + F_{1,2}, \tag{7}$$

with three scattering intensities corresponding to each individual dipole moment denoted by I_i and three interference terms of the form $F_{i,j}$. The scattering intensities are strictly positive valued, while the interference terms can be positive or negative, representing constructive or destructive interference, respectively. Figure 2c depicts the single dipole point spread functions (colored, solid) and summed interference (black, dashed) that contribute to the net image plane intensity distribution (black, solid) for the dipole state diagram in Figure 1g. We can see that the dominant dipole contribution comes from dipole 3, and that the overall interference is constructive, enhancing scattering.

The energy ordering and scattering intensities of the AuNRT normal modes reflect the observed blue shift and increase in scattering intensity with increasing polarization angle, providing insight into the roles of the dipole state and far-field interference. This interpretation relies on the fact that any state of the driven dipoles is a superposition of the three normal modes shown in Figures 2d–f. The normal modes of the coupled system are a superposition of the primitive modes of the constituent elements, forming a set of harmonic solutions to the coupled equations of motion. For the 1D oscillator model, we calculate three normal modes corresponding to 635, 677, and 702 nm excitation wavelengths, by solving the quasi-eigenvalue problem arising from Equation (1). Beneath the dipole state diagrams in Figure 2d-f are their corresponding image plane intensity distributions. These intensity distributions can be understood simply by noticing the dipoles in the 635 nm mode are mostly in phase and will constructively interfere while the

two smaller dipoles in the 702 nm mode oscillate out of phase with the center dipole, interfering destructively and reducing the net intensity.

The extent to which a pair of dipoles within the AuNRT model can interfere depends on their relative positions and orientations. We plot the interference between unit-amplitude dipole pairs representing either the two side dipoles or one side dipole with the central dipole in Figure 2g. Both configurations interfere most strongly at relative phases of 0° (in phase) and 180° (fully out of phase), with the central and side dipole interference having >2x the magnitude and the opposite sign as compared to the two side dipoles. The larger angular separation between the side dipoles produces a smaller overlap of their fields and subsequently smaller interference compared to the side and central dipole pair.

Results and Discussion

Trochoidal Intensity Modulation of AuNRTs

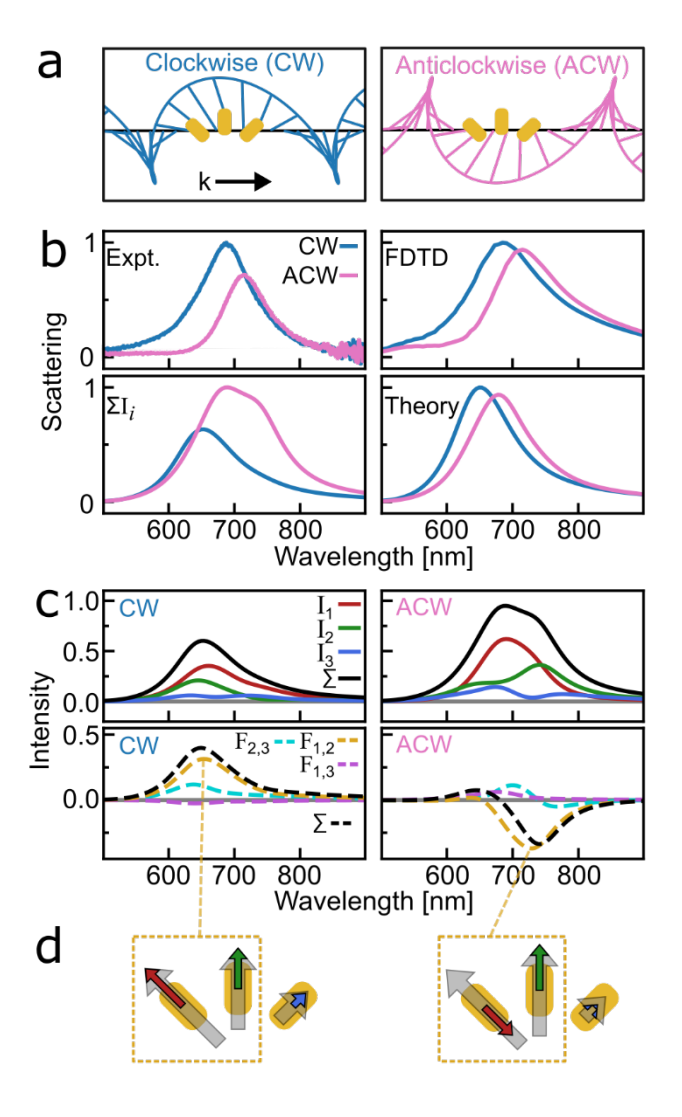


Figure 3. AuNRT trochoidal dichroism. (a) Trochoidal polarizations occur in evanescent waves, causing cartwheeling fields with clockwise (CW) or anticlockwise (ACW) direction. Experimental geometry leads to trochoidal polarizations with an asymmetric slant. AuNRT depicted to scale for reference. (b) Compared to CW, AuNRT scattering under ACW excitation is red shifted with an intensity decrease as measured in experiment and verified by FDTD simulation. The sum of single dipole contributions, $\sum I_i$, indicates that the dipole oscillator model is driven more strongly under ACW excitation, while theory incorporating far-field interference reproduces the dichroism observed in

experiment and FDTD simulation. (c) Breakdown of the theoretical scattering of AuNRTs into single dipole intensities (solid lines) and interference (dashed lines). Dominant single-dipole contribution is from dipole 1 under both polarizations. Dominant interference contribution under both polarizations is between dipoles 1 and 2, with a sign change from CW to ACW polarization. (d) Dipole state diagrams at the wavelength of maximum interference between dipoles 1 and 2 for CW and ACW polarizations. Under CW excitation dipoles 1 and 2 are fully in phase, while under ACW excitation dipoles 1 and 2 are almost 180° out of phase.

Trochoidal dichroism, which is dichroism of evanescent waves with opposite trochoidal polarizations⁵⁹ produced from total internal reflection of ±45° linearly polarized light,⁶⁰ has recently been demonstrated using L-shaped gold nanorod dimers.³⁵ Trochoidal polarizations are characterized by cartwheeling electric field distributions with longitudinal components. As such, the cartwheeling electric fields in trochoidal polarizations drive the AuNRT oscillator system in ways that cannot be achieved with linearly polarized light (Figure 3a, Supplementary Note 3). The rotational motion can be in clockwise (CW) or anticlockwise (ACW) directions. Trochoidal dichroism is the differential extinction of trochoidal polarizations of opposite rotational directions and can manifest as both scattering intensity modulation and resonance shifts when switching between CW and ACW excitation.

AuNRTs exhibit trochoidal dichroism with CW scattering peaked at a higher energy and with a higher intensity than for the ACW polarization due to far-field interference. FDTD simulations reproduce the experimental trochoidal dichroism as can be seen in the top row of Figure 3b, but do not explain the mechanisms underlying the observed spectra. For example, we have already shown that the scattering intensity alone does not explain how light couples to AuNRTs. Instead, the oscillator activity of the system, quantified by $\sum I_i$ in Figure 3b, reveals that the AuNRT is driven more strongly by the ACW polarization. With the incorporation of far-field interference, the scattering in Figure 3b calculated from the coupled-dipole model reverses, reproducing the drop in intensity for ACW incident polarization.

Interference between dipoles 1 and 2 leads to the decreased scattering intensity of AuNRTs under ACW polarization. Figure 3c breaks down the contributions to the net intensity in terms of the intensity from individual dipoles (top) and the interference between pairs of dipoles (bottom) for both CW and ACW light polarizations. For both polarizations, dipole 1 provides the largest single dipole contribution to the scattering intensity and the largest interference term is between dipoles 1 and 2. This interference term switches sign between the two polarizations due to an approximately 180° shift in the relative phase between dipoles 1 and 2. The dipole state diagrams in Figure 3d are calculated at the wavelengths of peak interference, as indicated by the dashed yellow lines that surround the associated dipoles. For CW polarization, all three dipoles oscillate in phase, similar to the normal mode in Figure 2d, and dipole 3 has the smallest oscillation amplitude, consistent with the slant of the CW trochoidal field illustrated in Figure 3a. For ACW polarization, dipole 1 is shifted ~180° out of phase with dipole 2. The oscillation amplitude of dipole 3 is further suppressed, despite the slant of the ACW field now aligning with dipole 3.

Tuning Trochoidal Intensity Dichroism via AuNRT Gap Size

In the absence of near-field coupling, the oscillation amplitudes of dipoles 1 and 3 are switched between CW and ACW polarizations. The slanted trochoidal fields discussed here (Figure 3a) contain a linear component that leads to single nanorods exhibiting an orientation dependent trochoidal intensity modulation that can be quantified as

$$I_{TDS} = \frac{I_{CW} - I_{ACW}}{\max\{I_{CW}, I_{ACW}\}}$$

using the difference between the peak scattering intensities, I_{CW} and I_{ACW} , for CW and ACW polarizations, respectively, and the maximum scattering intensity across both polarizations, $\max\{I_{CW}, I_{ACW}\}$. Figure 4a plots the orientation dependent I_{TDS} for a single nanorod as measured experimentally (red points) and calculated with a single dipole oscillator model (black line). The colored nanorod icons at the top of Figure 4a visually display nanorod orientation, and are color coded such that the red, green, and blue icons correspond to the AuNRT model dipoles 1, 2, and 3, respectively. Dipole 3

should be driven most strongly by ACW polarizations, leading to a correspondingly larger dipole oscillation amplitude. However, as shown in Figure 3c-d, when dipole 3 is considered in the context of the AuNRT model, this preferential scattering for ACW polarization does not materialize.

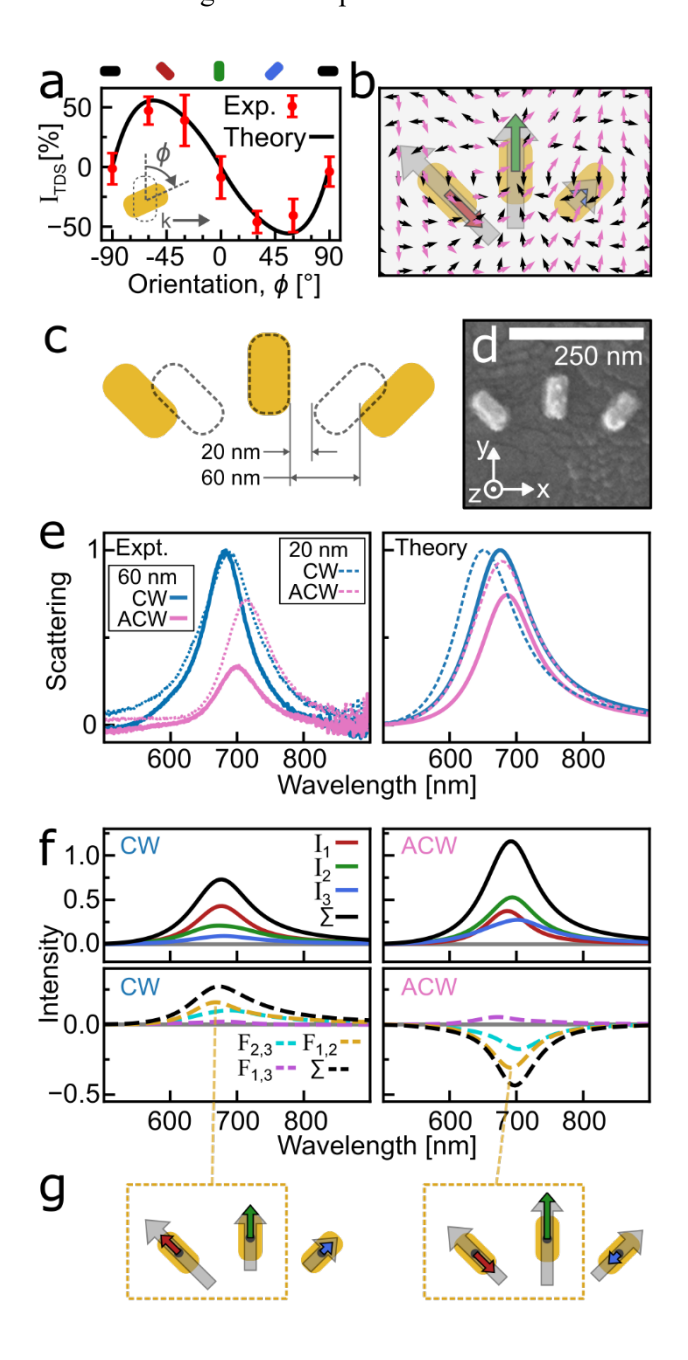


Figure 4. Increasing the gap size in AuNRTs decreases near-field coupling and increases intensity modulation. (a) 1D oscillator model of a nanorod under trochoidal excitation reproduces experimentally measured single nanorod trochoidal differential scattering intensity (I_{TDS}) for different

nanorod orientations. Dipoles 1 and 3 preferentially scatter CW and ACW polarizations, respectively. Experimental error bars represent standard deviations from the measurement of 8 single nanorods. (b) Vector field of the orientation of the electric field induced by dipole 2 (black) and external ACW field (pink). The electric field from dipole 2 opposes the ACW field in the region of dipole 3, while dipole 2 drives dipole 1 in the same direction as the ACW field. (c) Geometry of 60 nm gap AuNRT. (d) SEM micrograph of 60 nm gap AuNRT. (e) Trochoidal dichroism for 60 nm gap (solid lines) and 20 nm gap (dashed lines) AuNRTs. Theory correctly explains the decreased red shift and increased intensity modulation with increased gap size. (f) Breakdown of scattering contributions for CW and ACW polarizations. Compared to the 20 nm gap AuNRT under ACW excitation, the interference from dipoles 2 and 3 is now fully destructive, leading to the observed increase in intensity modulation. (g) Dipole moments at maximum interference between nanorods 1 and 2 for CW and ACW polarizations. Due to the decreased near-field coupling, dipole 3 is driven more strongly under ACW excitation for the 60 nm gap AuNRT as reflected by the length of the corresponding grey arrows.

The oscillation amplitude of dipole 3 is suppressed for ACW polarization due to near-field coupling from dipole 2. Figure 4b illustrates this effect with vector fields representing the incident ACW polarization (pink) and the field generated by dipole 2 (black) overlaid on the corresponding dipole state visualization. Due to the 1D oscillator formalism of our model, only the components of the electric fields directed parallel to the nanorod long axes contribute to dipole oscillation. Considering the vector field in the location of dipole 1, the external field and coupling field are additive, while for dipole 3 they are subtractive, leading to the dominance of dipole 1 for ACW polarization shown in Figure 3c-d. We can also see from Figure 4b that the orientation of the net electric field corresponds to the mostly head-to-tail phase relationship between dipoles 1 and 2, resulting in their destructive interference in the far field.

Increasing the gap size in AuNRTs decreases near-field coupling thereby decreasing the spectral shift, but at the same time tunes far-field interference that controls the trochoidal intensity modulation.

Altering the AuNRT geometry for a 60 nm corner-to-corner gap (Figure 4c-d) decreases the influence of near-field coupling due to the distance dependence of the dipole field.⁵⁵ In both the experimental and

model scattering spectra of Figure 4e, we see that the 60 nm gap AuNRT (solid lines) produces a smaller spectral shift and larger intensity modulation compared to the 20 nm gap AuNRT (dashed lines). The increase in intensity modulation is more pronounced in experimental spectra, but our theoretical model serves to provide insight into the behavior of the optical system. Figure S-5 compares scattering intensities for trochoidal polarizations with and without both near- and far-field effects, showing that the larger scattering peak for CW polarization is observed even when near-field coupling is set to zero, albeit without the spectral shift.

By inspecting the components of the scattering spectra (Figure 4f) and the dipole state (Figure 4g) we find that the increased intensity modulation of 60 nm gap AuNRTs arises from increased interference involving dipole 3 for both polarizations. Like the 20 nm gap AuNRTs in Figure 3c, the dominant interference term for 60 nm gap AuNRTs is between dipoles 1 and 2, and the term switches sign for opposite trochoidal polarizations. With increased gap size, the interference term between dipoles 2 and 3 now has an enhanced effect, behaving similarly to the interference between dipoles 1 and 2. While dipoles 1 and 3 do not switch oscillation amplitudes under opposite trochoidal polarizations as we observed in Figure 3a for single nanorods with the same orientations as dipoles 1 and 3, increasing the gap size limits near-field coupling and trends towards the uncoupled limit (Figure S-5).

Predictive Nanoantenna Design

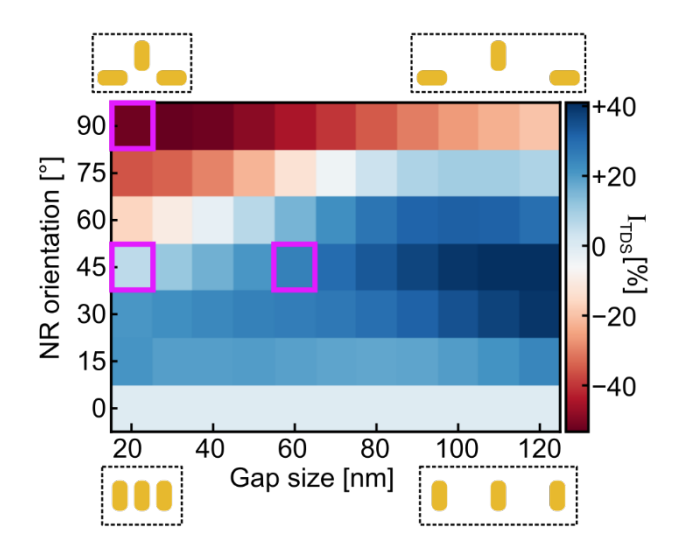


Figure 5. Geometry-dependent trochoidal dichroism can be predicted with a phase diagram derived from our coupled-dipole model. Illustrations of AuNRT geometry reflect the configurations at the corners of the phase diagram. Symmetrically changing the gap size and relative orientation of side nanorods reveals maximum positive I_{TDS} for 45° orientations and larger gap sizes. The most negative I_{TDS} occurs for 90° orientations and smaller gap sizes. AuNRT geometries discussed herein are indicated with pink boxes.

The coupled-dipole model predicts a reversal of trochoidal intensity modulation for AuNRTs with an increased angular offset, defined as the difference in orientation between the central and side nanorods. While fabricating mirror-image isomers provides one route to obtaining a reversed intensity modulation, this also leads to a reversed spectral shift.³⁵ To design a nanoantenna that reverses only the intensity modulation, we sweep over both gap size and angular offset to produce the phase diagram of predicted I_{TDS} shown in Figure 5. Pink boxes are used to mark the AuNRT geometries discussed herein. Simply varying the gap size for an angular offset of 45° does not lead to negative intensity modulation, but we predict that maximum ACW polarization-preferential intensity modulation is achieved with 90° angular offset AuNRTs with 20 nm gaps.

We test the predictions of our phase diagram in Figure 5 by altering the side nanorod orientations to tune the magnitude and sign of the far-field interference between pairs of nanorods. The interference trends for unit dipole pairs arranged according to the 90° AuNRT geometry are plotted in Figure 6a. We observe a few key differences when compared to the 45° AuNRT configuration (Figure 2g). Interference between dipoles 1 and 2 in Figure 6a is greatly suppressed and has the opposite positive-to-negative character due to the perpendicular orientation between dipoles 1 and 2. Meanwhile, dipoles 1 and 3 interfere more strongly in Figure 6a due to their colinear arrangement. Subsequently, the scattering intensity for 90° AuNRTs is expected to be dominated by interference between the side nanorods, unlike the case for 45° AuNRTs.

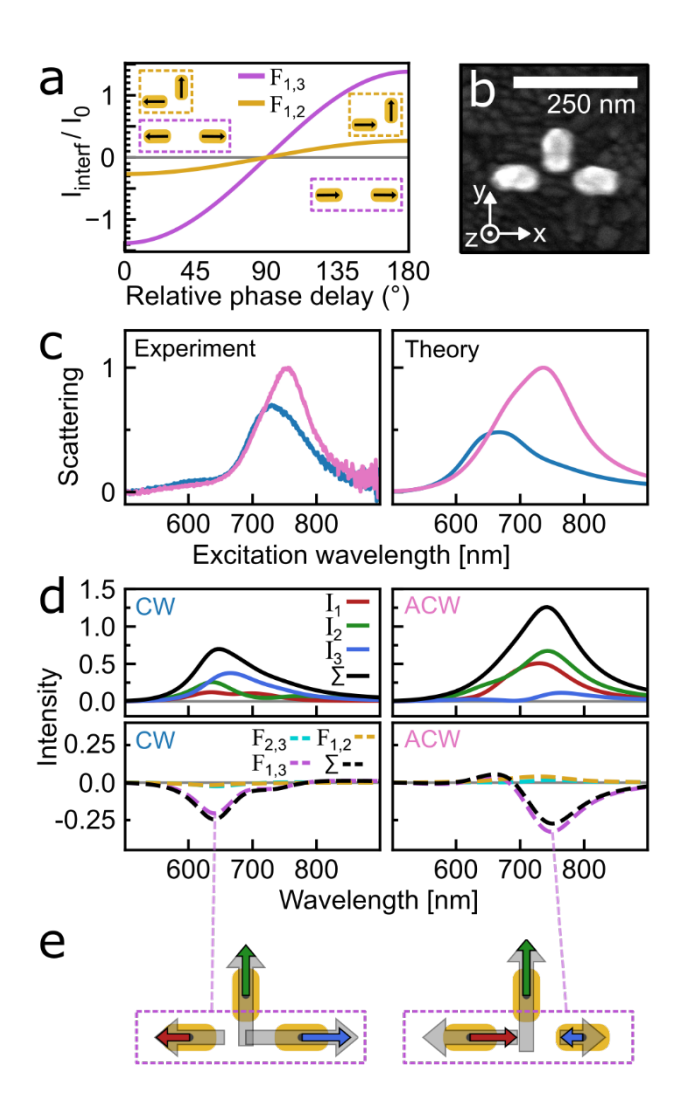


Figure 6. Far-field interference can be tuned by varying the angular offset in AuNRTs. (a)

Interference between pairs of nanorods (inset) isolated from the 90° AuNRT. (b) SEM micrograph of

AuNRT with 20 nm corner-to-corner gaps and 90° angular offset. (c) Trochoidal dichroism for a

representative AuNRT. Increasing the AuNRT angular offset to 90° reverses the trochoidal dichroism,

with scattering more strongly for ACW than CW excitation polarization. (d) Breakdown of scattering

contributions for CW and ACW polarizations. Compared to 20 nm gap AuNRTs with 45° angular offset,

the dominant interference for CW excitation comes from the destructive interference between dipoles 1

and 3. (e) Dipole moments at maximum interference between nanorod 1 and 3 for CW and ACW

polarizations.

AuNRTs with a 90° angular offset exhibit destructive interference under both CW and ACW polarizations. The experimental scattering for AuNRTs fabricated with a 20 nm gap size and a 90° angular offset (Figure 6b) produces reversed trochoidal intensity modulation in agreement with the coupled-dipole model (Figure 6c). The contributions to the scattering intensity shown in Figure 6d provide insight into the source of this reversed intensity modulation. $\sum I_i$ indicates that coupling between the 90° AuNRTs and incident field is strongest for ACW polarization, as is the case for the 45° AuNRTs. However, unlike the 45° AuNRTs, in the far-field the 90° AuNRTs undergo destructive interference for both polarizations. Due to weak interference involving the central nanorod (Figure 6a), the phase change of dipole 2 with opposite trochoidal polarizations does not strongly affect the scattering. Rather, the destructive interference between dipoles 1 and 3 oscillating mainly in phase (Figure 6g) dominates the scattering spectrum under both polarizations. By limiting the ability of the central nanorod to contribute to far-field interference, trochoidal dichroism of 90° AuNRT nanoantennas reflects the oscillator amplitudes of the system, resulting in preferential scattering under ACW excitation polarization.

Conclusions

In conclusion, we have established how simple coupled-dipole models can model and predict optical dichroism in AuNRT nanoantennas. The presented model incorporates both near-field interactions and far-field interference, and reproduces the optical dichroism of AuNRTs for both linear and cartwheeling trochoidal polarizations. For 45° AuNRTs, near-field coupling drives larger oscillation amplitudes for the ACW trochoidal field, while interference in the far field reduces the scattering intensity below that for the CW polarization. Trochoidal intensity modulation increases with gap size due to a decrease in near-field coupling. By utilizing the model to predict nanoantenna design, we fabricated AuNRTs with a 90° angular offset to reverse trochoidal intensity modulation while maintaining the direction of the spectral shift between scattering maxima for CW and ACW polarizations. Through this intuitive coupled-dipole model, we have demonstrated how understanding the role of near- and far-field effects allows us to design coupled nanoscale optical systems with tailored optical responses.

Materials and Methods

Single-particle spectroscopy. Single-particle scattering spectroscopy of AuNRTs and single nanorods was performed using an inverted dark-field microscope (Zeiss, Axio Observer, m1). To characterize the linear dichroism of AuNRTs, the particles were illuminated with unpolarized excitation from a tungsten halogen lamp (Zeiss, Axioline HAL 100). The excitation light passed through a 304-785 nm bandpass filter (Thorlabs FGS550) and was focused onto the sample with a dark-field condenser providing annular-symmetric excitation under total internal reflection conditions with a 68° angle of incidence. The light scattered from the particles was then collected with a 50x objective lens with a 0.8 numerical aperture (Zeiss, air-space). Light emerging from the body of the microscope was passed through a linear polarizer (Thorlabs LPVIS100) and was then directed to a hyperspectral imaging path that has been described elsewhere. In summary, the scattered light passed through a 20 μm slit aperture and then was dispersed by a spectrograph (Acton SpectraPro 2150i) and imaged onto a charge-coupled device camera (Princeton Instruments PIXIS BR 400), acquiring an image of intensity as a function of wavelength and position along the slit. The spectrograph and camera were mounted on a translation stage that was advanced across the field of view using a linear actuator (Newport LTA-HL). Additional spectrally resolved images were acquired at each step.

Trochoidal differential scattering experiments were performed using a fiber-coupled quartz tungsten halogen lamp (Newport 66884). Light from the lamp was filtered with a 304-785 nm bandpass filter (Thorlabs FGS550) and collimated with a 3 cm achromatic lens (Thorlabs AC254-030-A). The light was then linearly polarized at $\pm 45^{\circ}$ using a linear polarizer (Thorlabs LPVIS 100) and was focused onto an equilateral prism at an angle of $\sim 55^{\circ}$ using a 3 cm achromatic lens (Thorlabs AC254-030-A). Light scattered by the particles under $\pm 45^{\circ}$ incident polarizations was collected and characterized using a 50x air-space objective with a 0.8 numerical aperture (Zeiss) and the same hyperspectral detection system described above.

Electron-beam Lithography. AuNRTs were fabricated using electron beam lithography. All nanorods were designed to be 40 nm in width, 80 nm in length, and 40 nm in height. The corner-to-corner spacing between the nanorods varied from 20 nm to 60 nm. The angles of the side nanorods relative to the central rod were designed at 45° and 90° . The single nanorods were designed with the same size parameters and they were oriented at angles ranging from 0° to 180° relative to k incremented in 30 steps.

AuNRTs and single nanorods were prepared on ITO coated coverglass substrates (Delta Technology LTD CG-50IN-S107). The substrates were sonicated for ten minutes each in 2% V/V Hellmanex®/MilliQ water detergent, MilliQ water, and 190 proof ethanol. The substrates were then gently dried with N₂ and cleaned under an O₂ plasma for two minutes. After plasma cleaning, the substrates were coated in poly (methyl methacrylate) (PMMA), a positive-tone electron resist. The PMMA was used as purchased from Kayaku Advanced Materials (A4) and spin-coated onto the substrates at 4000 revolutions per minute for 60 seconds. The PMMA was then baked on a hotplate at 180°C for two minutes. After coating with PMMA, the samples were written with one of two electron beam systems, with no significant difference in sample quality (Figure S-6). The patterns were written with either an FEI Quanta 650 SEM with an incorporated nanometer pattern generation system or an Elionix® ELS-G100 SEM. The FEI Quanta 650 operated at 30 kV with a current of 40 pA and patterns were written with a dose of 500 μC/cm². The Elionix operated at 100 kV with a current of 1 nA and patterns were written with a dose of 1350 μC/cm².

The patterns were developed in a 1:3 mixture of methyl isobutyl ketone and isopropyl alcohol for 65 seconds and were then rinsed in isopropyl alcohol for 60 seconds before being dried under a stream of N₂. Then, 2 nm of Ti and 40 nm of Au were deposited onto the samples using an electron beam evaporator. Excess Ti and Au was removed by leaving the samples in acetone for 24 hours, followed by gentle, brief sonication and drying with N2.

FDTD simulations. Numerical electromagnetic simulations were performed with the Lumerical FDTD module. Gold nanorods (rectangular prisms, 80×40×40 nm), are positioned on a glass substrate

with a 160 nm thick ITO layer. The refractive index of gold is extracted from Johnson-Christy and the refractive index of glass is set to 1.52. The refractive index of ITO is approximately 1.7, with a wavelength dependence obtained from Ref. ⁶². Linearly polarized fields were generated using an oblique plane wave excitation source with a 40° angle of incidence. To generate trochoidal evanescent fields, we used an oblique plane wave excitation source with a 55° angle of incidence to produce total internal reflection at the glass-air boundary. The effect of collection angle on the optical microscope is considered by using a rectangular aperture collecting the same amount of power as the collection objective on the experimental setup.

AuNRT modeling. AuNRTs were modeled as three coupled point dipole oscillators with polarizability tensors calculated from the prolate spheroid approximation (Supplementary Note 1). The point dipoles were reduced to 1D oscillators by retaining the longitudinal component of the polarizability tensor and setting the other components to zero. Near-field coupling was accounted for by the superposition of the external field with the dipole fields generated by the nearest neighbors of each constituent dipole in the AuNRT. The normal modes of the AuNRT were calculated using the 1D polarizability tensor and including near-field coupling between all dipoles. A more complete discussion of the normal mode calculation is included in Supplementary Note 4 and the normal modes for the designed AuNRT geometries are included in Figure S-7. Image plane electric field distributions for each dipole scatterer were calculated using an analytical approximation of the Debye-Wolf diffraction integrals as described in Ref. 43.

ACKNOWLEDGEMENT

Funding for this work was provided by the Robert A. Welch Foundation to C.F.L. (C-1787) and to S.L. (C-1664) and the National Science Foundation to S.L. (CHE-1727122) and D.J.M. (CHE-1727092). L.A.M. gratefully acknowledges support from the National Science Foundation Graduate

Research Fellowship Program (1842494). This work was conducted in part using resources of the Shared Equipment Authority at Rice University.

AUTHOR INFORMATION

Corresponding Author

* Corresponding author E-mails: David J. Masiello: masiello@uw.edu, Stephan Link: slink@rice.edu, Christy F. Landes: cflandes@rice.edu,

Author Contributions

The manuscript was written through contributions of all authors. All authors have given approval to the final version of the manuscript.

Conflicts of interest

There are no conflicts of interest to declare.

ASSOCIATED CONTENT

Supporting Information

The Supporting Information is available free of charge at https://pubs.acs.org/doi/

Discussion of nanorod polarizability modeling, fitting nanorod scattering spectra, alternate polarizability models, dyadic Green's function formulism, BEM simulations for decreasing gap size in nanorod dimers, FDTD simulation of linearly polarized scattering, scattering peak wavelengths for linear polarizations, equations for trochoidal field polarizations, separation of near- and far-field effects,

26

comparison of AuNRT fabrication techniques, discussion of normal mode analysis, and normal modes for alternate AuNRT geometries.

References

- 1. Halas, N. J.; Lal, S.; Chang, W. S.; Link, S.; Nordlander, P., Plasmons in strongly coupled metallic nanostructures. *Chem. Rev.* **2011**, *111*, 3913-61.
- 2. Kelly, K. L.; Coronado, E.; Zhao, L. L.; Schatz, G. C., The optical properties of metal nanoparticles: The influence of size, shape, and dielectric environment. *J. Phys. Chem. B* **2003**, *107*, 668-677.
- 3. Gansel, J. K.; Thiel, M.; Rill, M. S.; Decker, M.; Bade, K.; Saile, V.; Freymann, G. v.; Linden, S.; Wegener, M., Gold Helix Photonic Metamaterial as Broadband Circular Polarizer. *Science* **2009**, *325*, 1513-1515.
- 4. Hentschel, M.; Schäferling, M.; Duan, X.; Giessen, H.; Liu, N., Chiral plasmonics. *Sci. Adv.* **2017,** *3*, e1602735.
- 5. Hentschel, M.; Schäferling, M.; Weiss, T.; Liu, N.; Giessen, H., Three-Dimensional Chiral Plasmonic Oligomers. *Nano Lett.* **2012**, *12*, 2542-2547.
- 6. Baker, T. A.; Grubisic, A.; Nesbitt, D. J., Plasmon Mediated Multiphoton Photoemission Microscopy of Au Nanoholes and Nanohole Dimers. *J. Phys. Chem. C* **2014**, *118*, 6959-6971.
- 7. Liu, N.; Liedl, T., DNA-Assembled Advanced Plasmonic Architectures. *Chem. Rev.* **2018**, *118*, 3032-3053.
- 8. Stockman, M. I., Nanoplasmonic sensing and detection. *Science* **2015**, *348*, 287-8.
- 9. Haynes, C. L.; McFarland, A. D.; Van Duyne, R. P., Surface-enhanced Raman spectroscopy. *Anal. Chem.* **2005**, *77*, 338a-346a.
- 10. Stiles, P. L.; Dieringer, J. A.; Shah, N. C.; Van Duyne, R. P., Surface-enhanced Raman spectroscopy. *Annu. Rev. Anal. Chem.* **2008**, *1*, 601-26.
- 11. Hao, E.; Schatz, G. C., Electromagnetic fields around silver nanoparticles and dimers. *J. Chem. Phys.* **2004**, *120*, 357-66.
- 12. Zhang, X.; Chen, Y. L.; Liu, R. S.; Tsai, D. P., Plasmonic photocatalysis. *Rep. Prog. Phys.* **2013**, 76, 046401.
- 13. Andoy, N. M.; Zhou, X.; Choudhary, E.; Shen, H.; Liu, G.; Chen, P., Single-molecule catalysis mapping quantifies site-specific activity and uncovers radial activity gradient on single 2D nanocrystals. *J. Am. Chem. Soc.* **2013**, *135*, 1845-52.
- 14. Li, K.; Hogan, N. J.; Kale, M. J.; Halas, N. J.; Nordlander, P.; Christopher, P., Balancing Near-Field Enhancement, Absorption, and Scattering for Effective Antenna-Reactor Plasmonic Photocatalysis. *Nano Lett.* **2017**, *17*, 3710-3717.
- 15. Han, Z.; Bozhevolnyi, S. I., Radiation guiding with surface plasmon polaritons. *Rep. Prog. Phys.* **2013,** *76*, 016402.
- 16. Fang, Y. R.; Sun, M. T., Nanoplasmonic waveguides: towards applications in integrated nanophotonic circuits. *Light: Sci. Appl.* **2015**, *4*, e294-e294.
- 17. Bozhevolnyi, S. I.; Volkov, V. S.; Devaux, E.; Laluet, J. Y.; Ebbesen, T. W., Channel plasmon subwavelength waveguide components including interferometers and ring resonators. *Nature* **2006**, *440*, 508-11.
- 18. Lal, S.; Link, S.; Halas, N. J., Nano-optics from sensing to waveguiding. *Nat. Photonics* **2007**, *1*, 641-648.
- 19. Anger, P.; Bharadwaj, P.; Novotny, L., Enhancement and quenching of single-molecule fluorescence. *Phys. Rev. Lett.* **2006**, *96*, 113002.

- 20. Tam, F.; Goodrich, G. P.; Johnson, B. R.; Halas, N. J., Plasmonic enhancement of molecular fluorescence. *Nano Lett.* **2007**, *7*, 496-501.
- 21. Donehue, J. E.; Wertz, E.; Talicska, C. N.; Biteen, J. S., Plasmon-Enhanced Brightness and Photostability from Single Fluorescent Proteins Coupled to Gold Nanorods. *J. Phys. Chem. C* **2014**, *118*, 15027-15035.
- 22. Khatua, S.; Paulo, P. M.; Yuan, H.; Gupta, A.; Zijlstra, P.; Orrit, M., Resonant plasmonic enhancement of single-molecule fluorescence by individual gold nanorods. *ACS Nano* **2014**, *8*, 4440-9.
- Wertz, E. A.; Isaacoff, B. P.; Biteen, J. S., Wavelength-Dependent Super-resolution Images of Dye Molecules Coupled to Plasmonic Nanotriangles. *ACS Photonics* **2016**, *3*, 1733-1740.
- 24. Raab, M.; Vietz, C.; Stefani, F. D.; Acuna, G. P.; Tinnefeld, P., Shifting molecular localization by plasmonic coupling in a single-molecule mirage. *Nat. Commun.* **2017**, *8*, 13966.
- 25. Ropp, C.; Cummins, Z.; Nah, S.; Fourkas, J. T.; Shapiro, B.; Waks, E., Nanoscale probing of image-dipole interactions in a metallic nanostructure. *Nat. Commun.* **2015**, *6*, 6558.
- 26. Su, L.; Lu, G.; Kenens, B.; Rocha, S.; Fron, E.; Yuan, H.; Chen, C.; Van Dorpe, P.; Roeffaers, M. B.; Mizuno, H.; Hofkens, J.; Hutchison, J. A.; Uji, I. H., Visualization of molecular fluorescence point spread functions via remote excitation switching fluorescence microscopy. *Nat. Commun.* **2015**, *6*, 6287.
- 27. Baiyasi, R.; Jebeli, S. A. H.; Zhang, Q.; Su, L.; Hofkens, J.; Uji-i, H.; Link, S.; Landes, C. F., PSF Distortion in Dye–Plasmonic Nanomaterial Interactions: Friend or Foe? *ACS Photonics* **2019**, *6*, 699-708.
- 28. Zuo, T.; Goldwyn, H. J.; Isaacoff, B. P.; Masiello, D. J.; Biteen, J. S., Rotation of Single-Molecule Emission Polarization by Plasmonic Nanorods. *J. Phys. Chem. Lett.* **2019**, *10*, 5047-5054.
- 29. Schnell, M.; Alonso-Gonzalez, P.; Arzubiaga, L.; Casanova, F.; Hueso, L. E.; Chuvilin, A.; Hillenbrand, R., Nanofocusing of mid-infrared energy with tapered transmission lines. *Nat. Photonics* **2011,** *5*, 283-287.
- 30. Curto, A. G.; Volpe, G.; Taminiau, T. H.; Kreuzer, M. P.; Quidant, R.; van Hulst, N. F., Unidirectional emission of a quantum dot coupled to a nanoantenna. *Science* **2010**, *329*, 930-3.
- 31. Hübner, K.; Pilo-Pais, M.; Selbach, F.; Liedl, T.; Tinnefeld, P.; Stefani, F. D.; Acuna, G. P., Directing Single-Molecule Emission with DNA Origami-Assembled Optical Antennas. *Nano Lett.* **2019**, *19*, 6629-6634.
- 32. Kinkhabwala, A.; Yu, Z. F.; Fan, S. H.; Avlasevich, Y.; Mullen, K.; Moerner, W. E., Large single-molecule fluorescence enhancements produced by a bowtie nanoantenna. *Nat. Photonics* **2009**, *3*, 654-657.
- 33. Yin, X.; Schaferling, M.; Metzger, B.; Giessen, H., Interpreting chiral nanophotonic spectra: the plasmonic Born-Kuhn model. *Nano Lett.* **2013**, *13*, 6238-43.
- 34. Kuzyk, A.; Schreiber, R.; Fan, Z.; Pardatscher, G.; Roller, E. M.; Hogele, A.; Simmel, F. C.; Govorov, A. O.; Liedl, T., DNA-based self-assembly of chiral plasmonic nanostructures with tailored optical response. *Nature* **2012**, *483*, 311-4.
- 35. McCarthy, L. A.; Smith, K. W.; Lan, X.; Hosseini Jebeli, S. A.; Bursi, L.; Alabastri, A.; Chang, W. S.; Nordlander, P.; Link, S., Polarized evanescent waves reveal trochoidal dichroism. *Proc. Natl. Acad. Sci.* **2020**, *117*, 16143-16148.
- 36. Zhang, Q.; Hernandez, T.; Smith, K. W.; Hosseini Jebeli, S. A.; Dai, A. X.; Warning, L.; Baiyasi, R.; McCarthy, L. A.; Guo, H.; Chen, D. H.; Dionne, J. A.; Landes, C. F.; Link, S., Unraveling the origin of chirality from plasmonic nanoparticle-protein complexes. *Science* **2019**, *365*, 1475-1478.
- 37. Yin, X.; Schäferling, M.; Metzger, B.; Giessen, H., Interpreting Chiral Nanophotonic Spectra: The Plasmonic Born–Kuhn Model. *Nano Lett.* **2013**, *13*, 6238-6243.
- 38. Hendry, E.; Carpy, T.; Johnston, J.; Popland, M.; Mikhaylovskiy, R. V.; Lapthorn, A. J.; Kelly, S. M.; Barron, L. D.; Gadegaard, N.; Kadodwala, M., Ultrasensitive detection and characterization of biomolecules using superchiral fields. *Nat. Nanotechnol.* **2010**, *5*, 783-787.
- 39. Smith, K. W.; McCarthy, L. A.; Alabastri, A.; Bursi, L.; Chang, W. S.; Nordlander, P.; Link, S., Exploiting Evanescent Field Polarization for Giant Chiroptical Modulation from Achiral Gold Half-Rings. *ACS Nano* **2018**, *12*, 11657-11663.

- 40. Gansel, J. K.; Thiel, M.; Rill, M. S.; Decker, M.; Bade, K.; Saile, V.; von Freymann, G.; Linden, S.; Wegener, M., Gold Helix Photonic Metamaterial as Broadband Circular Polarizer. *Science* **2009**, *325*, 1513-1515.
- 41. Bharadwaj, P.; Deutsch, B.; Novotny, L., Optical Antennas. *Adv. Opt. Photonics* **2009**, *1*, 438-483.
- 42. Esmann, M.; Becker, S. F.; Witt, J.; Zhan, J.; Chimeh, A.; Korte, A.; Zhong, J.; Vogelgesang, R.; Wittstock, G.; Lienau, C., Vectorial near-field coupling. *Nat. Nanotechnol.* **2019**, *14*, 698-704.
- 43. Goldwyn, H. J.; Smith, K. C.; Busche, J. A.; Masiello, D. J., Mislocalization in Plasmon-Enhanced Single-Molecule Fluorescence Microscopy as a Dynamical Young's Interferometer. *ACS Photonics* **2018**, *5*, 3141-3151.
- 44. Auguié, B.; Barnes, W. L., Collective resonances in gold nanoparticle arrays. *Phys. Rev. Lett.* **2008**, *101*, 143902.
- 45. Bhattacharjee, U.; West, C. A.; Hosseini Jebeli, S. A.; Goldwyn, H. J.; Kong, X. T.; Hu, Z.; Beutler, E. K.; Chang, W. S.; Willets, K. A.; Link, S.; Masiello, D. J., Active Far-Field Control of the Thermal Near-Field via Plasmon Hybridization. *ACS Nano* **2019**, *13*, 9655-9663.
- 46. Fan, Z.; Govorov, A. O., Plasmonic circular dichroism of chiral metal nanoparticle assemblies. *Nano Lett.* **2010**, *10*, 2580-7.
- 47. Chen, T.; Yao, Q.; Yuan, X.; Nasaruddin, R. R.; Xie, J., Heating or Cooling: Temperature Effects on the Synthesis of Atomically Precise Gold Nanoclusters. *J. Phys. Chem. C* **2016**, *121*, 10743-10751.
- 48. Nan, F.; Yan, Z., Optical Sorting at the Single-Particle Level with Single-Nanometer Precision Using Coordinated Intensity and Phase Gradient Forces. *ACS Nano* **2020**, *14*, 7602-7609.
- 49. Liu, Y.; Li, Y.; Jeong, S.; Wang, Y.; Chen, J.; Ye, X., Colloidal Synthesis of Nanohelices via Bilayer Lattice Misfit. *J. Am. Chem. Soc.* **2020**, *142*, 12777-12783.
- 50. Mahmoud, M. A., Tunable Plasmonic Neutral Density Filters and Chromatic Polarizers: Highly Packed 2D Arrays of Plasmonic Nanoparticle on Elastomer Substrate. *J. Phys. Chem. C* **2016**, *120*, 18249-18258.
- 51. Weller, L.; Thacker, V. V.; Herrmann, L. O.; Hemmig, E. A.; Lombardi, A.; Keyser, U. F.; Baumberg, J. J., Gap-Dependent Coupling of Ag–Au Nanoparticle Heterodimers Using DNA Origami-Based Self-Assembly. *ACS Photonics* **2016**, *3*, 1589-1595.
- 52. Kuzyk, A.; Schreiber, R.; Zhang, H.; Govorov, A. O.; Liedl, T.; Liu, N., Reconfigurable 3D plasmonic metamolecules. *Nat. Mater.* **2014**, *13*, 862-6.
- 53. Zhou, L.; Tan, Y.; Ji, D.; Zhu, B.; Zhang, P.; Xu, J.; Gan, Q.; Yu, Z.; Zhu, J., Self-assembly of highly efficient, broadband plasmonic absorbers for solar steam generation. *Sci. Adv.* **2016**, *2*, e1501227.
- 54. Moroz, A., Depolarization field of spheroidal particles. *J. Opt. Soc. Am. B* **2009,** *26*, 517-527.
- 55. Novotny, L.; Hecht, B., *Principles of Nano-Optics*. 2nd ed., 25-30; Cambridge University Press: 2012.
- 56. Chang, W. S.; Lassiter, J. B.; Swanglap, P.; Sobhani, H.; Khatua, S.; Nordlander, P.; Halas, N. J.; Link, S., A plasmonic Fano switch. *Nano Lett.* **2012**, *12*, 4977-82.
- 57. Smith, K. W.; Yang, J.; Hernandez, T.; Swearer, D. F.; Scarabelli, L.; Zhang, H.; Zhao, H.; Moringo, N. A.; Chang, W.-S.; Liz-Marzán, L. M.; Ringe, E.; Nordlander, P.; Link, S., Environmental Symmetry Breaking Promotes Plasmon Mode Splitting in Gold Nanotriangles. *J. Phys. Chem. C* **2017**, *122*, 13259-13266.
- 58. Balanis, C. A., Antenna Theory: Analysis and Design. 4th ed., 141-144; Wiley: 2016.
- 59. Bliokh, K. Y.; Bekshaev, A. Y.; Nori, F., Extraordinary momentum and spin in evanescent waves. *Nat. Commun.* **2014**, *5*, 3300.
- 60. Bliokh, K. Y.; Nori, F., Transverse and longitudinal angular momenta of light. *Phys. Rep.* **2015**, 592, 1-38.
- 61. Byers, C. P.; Hoener, B. S.; Chang, W. S.; Yorulmaz, M.; Link, S.; Landes, C. F., Single-particle spectroscopy reveals heterogeneity in electrochemical tuning of the localized surface plasmon. *J. Phys. Chem. B* **2014**, *118*, 14047-55.

62. Konig, T. A.; Ledin, P. A.; Kerszulis, J.; Mahmoud, M. A.; El-Sayed, M. A.; Reynolds, J. R.; Tsukruk, V. V., Electrically tunable plasmonic behavior of nanocube-polymer nanomaterials induced by a redox-active electrochromic polymer. *ACS Nano* **2014**, *8*, 6182-92.

For Table of Contents Use Only

Title: Coupled Dipole Modeling and Experimental Characterization of Geometry-Dependent Trochoidal Dichroism in Nanorod Trimers

Authors: Rashad Baiyasi, Harrison J. Goldwyn, Lauren A. McCarthy, Claire A. West, Seyyed Ali Hosseini Jebeli, David J. Masiello, Stephan Link, Christy F. Landes

Description of TOC figure: Cartwheeling trochoidal polarizations differentially scatter from gold nanorod trimers due to the near-field coupling between oscillating dipoles and far-field interference in the image plane.

